Range Condition and ML-EM Checkerboard Artifacts

Jiangsheng You, *Member, IEEE*, Jing Wang, and Zhengrong Liang, *Fellow, IEEE*

***Abstract*—The expectation maximization (EM) algorithm for the maximum likelihood (ML) image reconstruction criterion generates severe checkerboard artifacts in the presence of noise. A classical remedy is to impose an *a priori* constraint for a penalized ML or maximum *a posteriori* probability solution. The penalty reduces the checkerboard artifacts and also introduces uncertainty because *a priori* information is usually unknown in clinic. Recent theoretical investigation reveals that the noise can be divided into two components: one is called null-space noise and the other is range-space noise. The null-space noise can be numerically estimated using filtered backprojection (FBP) algorithm. By the FBP algorithm, the null-space noise annihilates in the reconstruction while the range-space noise propagates into the reconstructed image. The aim of this work is to investigate the relation between the null-space noise and the checkerboard artifacts in the ML-EM reconstruction from noisy projection data. Our study suggests that removing the null-space noise from the projection data could improve the signal-to-noise ratio of the projection data and, therefore, reduce the checkerboard artifacts in the ML-EM reconstructed images. This study reveals an in-depth understanding of the different noise propagations in analytical and iterative image reconstructions, which may be useful to single photon emission computed tomography, where the noise has been a major factor for image degradation. The reduction of the ML-EM checkerboard artifacts by removing the null-space noise avoids the uncertainty of using *a priori* penalty.**

***Index Terms*—Attenuated Radon transform, computed tomography, consistent condition, noise analysis, SPECT.**

I. Introduction

THE projection data in single photon emission computed tomography (SPECT) is mathematically described by the attenuated Radon transform (aRT) [1]. The corresponding image reconstruction is to invert the transform. Recently, an explicit filtered backprojection (FBP)-type inversion formula was derived by Novikov [2], indicating that the compensation for non-uniform attenuation can be performed with an analytical reconstruction algorithm besides iterative reconstruction methods in the literature. Especially the range condition of the aRT was obtained in [3] to characterize the consistency of the projection data. This work aims to relate the range condition of the aRT to the well-known checkerboard artifacts in the maximum-likelihood expectation-maximization (ML-EM) reconstruction algorithm [4]–[7]. The presentation of this work is organized as follows. In Section II, some basics about the aRT are reviewed in two dimensions for a preliminary. In Section III, the ML-EM approach to the inversion of the attenuated Radon transform is outlined briefly. In Section IV, we describe the range condition of the aRT. The relation between the range condition and the checkerboard artifacts is numerically demonstrated in Section V, followed by discussion and conclusion in Section VI.

Manuscript received November 13, 2006; revised March 23, 2007. The work of Z. Liang was supported in part by the U.S. NIH under Grant No. CA082402.

J. You is with Cubic Imaging LLC, Auburndale, MA 02466 USA, and also with the Department of Radiology, State University of New York, Stony Brook, NY 11794 USA (e-mail: jyou@cubic-imaging.com).

J. Wang is with Departments of Radiology and Physics & Astronomy, State University of New York, Stony Brook, NY 11794 USA (e-mail: jingwang@mil.sunysb.edu).

Z. Liang is with Departments of Radiology and Computer Science, State University of New York, Stony Brook, NY 11794 USA (e-mail: jzl@mil.sunysb.edu).

Color versions of one or more of the figures in this paper are available online at http://ieeexplore.ieee.org.

Digital Object Identifier 10.1109/TNS.2007.901198

II. Attenuated Radon Transform and Measurement Noise

Denote by R^2 the two-dimensional (2D) planar space with coordinate representation (x, y) in the Cartesian system and (r, φ) in the polar system, and S^1 the unit circle represented by $\vec{\theta} = (\cos\theta, \sin\theta)$ with $\theta \in [0, 2\pi)$. Assume $f(x, y)$ is a function of R^2 and

$$f_\theta(s,t) = f(s\cos\theta - t\sin\theta, s\sin\theta + t\cos\theta) \tag{1}$$

stands for the same function in the Cartesian coordinates $(s, t)_\theta$ after rotation by an angle θ along the counterclockwise direction. The coordinates $(s, t)_\theta$ and (x, y) are related by

$$\begin{pmatrix} s \\ t \end{pmatrix} = \begin{pmatrix} \cos\theta & \sin\theta \\ -\sin\theta & \cos\theta \end{pmatrix} \begin{pmatrix} x \\ y \end{pmatrix} \quad \text{and} \quad \begin{pmatrix} x \\ y \end{pmatrix} = \begin{pmatrix} \cos\theta & -\sin\theta \\ \sin\theta & \cos\theta \end{pmatrix} \begin{pmatrix} s \\ t \end{pmatrix}. \tag{2}$$

Considering that (x, y) is defined for the static object while $(s, t)_\theta$ is associated with the rotating detector, we call (x, y) the object coordinates and $(s, t)_\theta$ the detector coordinates.

In SPECT imaging, function $f(x, y)$ represents the radiotracer concentration distribution inside the human body tissues. Gamma photons emitted at position (x, y) inside the body are linearly attenuated by the body tissues before they arrive at location $(s, t)_\theta$ on the detector surface. Let $\mu(x, y)$ stand for the distribution of linear attenuation coefficients and $p(s, \theta)$ be the accumulated photon counts at s along the view angle θ in the coordinates $(s, t)_\theta$, projection $p(s, \theta)$ is expressed as

$$p(s,\theta) = \int_{-\infty}^{\infty} f_\theta(s,\tau) e^{-a_\theta(s,\tau)} d\tau \tag{3}$$

where $a_\theta(s, \tau) = \int_\tau^\infty \mu_\theta(s, t) dt$. Equation (3) is the so-called attenuated Radon transform of $f(x, y)$, and is denoted by $\mathbf{R}_\mu f$. Due to the limited-photon counting statistics in SPECT imaging,

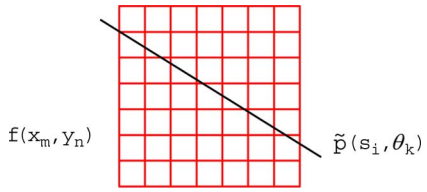

Fig. 1. Discrete view of projection data and image array.

the projection measurements are noisy and may be decomposed into

$$\widetilde{p}(s,\theta) = p(s,\theta) + n(s,\theta) \tag{4}$$

where $n(s,\theta)$ represents the Poisson noise which is dependent on the mean projection $p(s,\theta)$. Because of the Poisson nature of photon counting statistics, $\widetilde{p}(s,\theta)$ is usually assumed to be a Poisson-point process. More properties of the Poisson-point process can be found in [8]. Assuming that attenuation map $\mu(x,y)$ is known and projection measurement $\widetilde{p}(s,\theta)$ is available, the goal of SPECT image reconstruction is to estimate $f(x,y)$ from the mean projection (3) or the noisy projection (4). This topic has been investigated for several decades using a variety of different methods. There are mainly two classes of methods for the image reconstruction from projections. One class consists of analytical algorithms which are based on exact inversion formulas in continuous space, for example the algorithm of [9] if the attenuation is ignored, [10] if the attenuation is uniform, and [2] if the attenuation is non-uniform, after the noise is filtered. The other class consists of iterative algorithms which model the relation between object function $f(x,y)$ and the noisy data $\widetilde{p}(s,\theta)$ as a cost function or criterion in the discrete space and minimize the cost function for image reconstruction. The EM algorithm for the ML criterion is one of the most important iterative methods.

III. ML-EM Image Reconstruction and Checkerboard Artifacts

Let us first discuss the discrete version of (3) and (4). Denote by $\widetilde{p}_{i,k} = \widetilde{p}(s_i,\theta_k)$ a set of acquired projections at detector bin locations (s_i,θ_k) and $f_{m,n} = f(x_m,y_n)$ the discrete image to be reconstructed in the object coordinates. Fig. 1 gives an illustrative view on the discrete image $f_{m,n}$, a projection ray $\widetilde{p}_{i,k}$ at view angle θ_k, and a lateral position s_i on the detector surface. Let $c_{m,n}^{i,k}$ denote the fraction of each $f_{m,n}$ contributing to the projection $\widetilde{p}_{i,k}$. Note that $c_{m,n}^{i,k}$ can be calculated by using the pixel array (x_m,y_n) and the detector bin location (s_i,θ_k) and may include the attenuation and other image degradation factors such as collimator response and scattering. The discrete version of (3) and (4) can be expressed as

$$\widetilde{p}_{i,k} = \sum_{m,n} c_{m,n}^{i,k} f_{m,n} + n_{i,k} \tag{5}$$

where $n_{i,k} = n(s_i,\theta_k)$ is the noise. In SPECT imaging, $\widetilde{p}_{i,k}$ takes non-negative integer numbers representing the photon counts.

Obviously, one may directly solve the linear equation system (5) as the algebraic reconstruction technique does [11], assuming that the noise can be either ignored or has been filtered. By the known Poisson nature of the noisy data, a statistical approach of modeling the noise property would be preferred. The well-known ML criterion is defined as:

$$L = \prod_{k,i} e^{-\sum_{m,n} c_{m,n}^{i,k} f_{m,n}} \left[\sum_{m,n} c_{m,n}^{i,k} f_{m,n}\right]^{\widetilde{p}_{i,k}} \Big/ \widetilde{p}_{i,k}!. \tag{6}$$

The goal of the ML approach is to look for $f_{m,n}$ such that L arrives at the maximum for a given set of acquisition $\widetilde{p}_{i,k}$ and the system matrix $\{c_{m,n}^{i,k}\}$. One of the most important iterative schemes for the ML image reconstruction is the EM algorithm [5]. The ML-EM algorithm suggests the following simple iterative scheme to reach the maximum point of (6)

$$f_{m,n}^{(j+1)} = \frac{f_{m,n}^{(j)}}{\sum_{i,k} c_{m,n}^{i,k}} \sum_{i,k} c_{m,n}^{i,k} \frac{\widetilde{p}_{i,k}}{\sum_{m,n} c_{m,n}^{i,k} f_{m,n}^{(j)}}, \quad j = 0,1,\cdots, \tag{7}$$

where $f_{m,n}^{(j)}$ is the reconstruction from the jth iteration. Many attractive features of the iterative scheme (7) can be found in [5] and [6].

The ML-EM reconstruction algorithm (7) diverges for large number of iterations with severe checkerboard artifacts when noise is present in the projection data [4]. Without a noise-reduction strategy, the reconstructed image from (7) does not appear to be clinically useful. In order to mitigate the artifacts, Bayesian criterion was introduced in [12]. By regularization techniques such as an *a priori* constraint or a penalty function, the ML criterion (6) may be rewritten as the maximum *a posteriori* (MAP) criterion:

$$L_1 = \ln\left\{\prod_{k,i} e^{-\sum_{m,n} c_{m,n}^{i,k} f_{m,n}} \left[\sum_{m,n} c_{m,n}^{i,k} f_{m,n}\right]^{\widetilde{p}_{i,k}} \Big/ \widetilde{p}_{i,k}!\right\} - U\left[f_{m,n} - f_{m',n'}, \alpha(f)\right] \tag{8}$$

where $U(\cdot)$ stands for *a priori* information and is usually expressed as a potential function on the neighborhood system, i.e., index (m',n') specifies the neighbors around (m,n) and $\alpha(f)$ may reflect any known information about the radiotracer concentration distribution [12]. By the use of the EM algorithm, an iterative MAP-EM scheme to reach the maximum point of (8) can also be derived [12]. The penalty reduces the checkerboard artifacts and also introduces uncertainty because the *a priori* information is usually unknown in clinic. In the past decades, a great effort has been devoted to investigate the propagation of noise $n(s,\theta)$ in the reconstructed images by the iterative ML-EM and MAP-EM methods [13]–[18]. One of the difficulties in these investigations is the high non-linearity of the ML-EM and MAP-EM algorithms, approximations have to be made to simplify the mathematical arguments. Recent theoretical investigation on the FBP-type inversion of the aRT reveals more insight into the noise propagation issue. In this paper, we use the FBP-type inversion to analyze the noise propagation in the ML-EM image reconstruction.

IV. FBP-Type Algorithm and Range Condition

Since Novikov derived the FBP-type inversion formula for the aRT [2], a great research effort has been devoted to investigate the noise properties of that FBP-type algorithm, e.g., [3]. Before introducing the Novikov's inversion formula, we give the definition of two well-known transforms. One is the Hilbert transform, which is defined as

$$[\mathbf{H}g](s) = \frac{1}{\pi}\mathrm{pv}\int_{-\infty}^{\infty}\frac{g(l)}{s-l}dl \tag{9}$$

where "pv" stands for the principal value integral. The other is the Radon transform as defined by

$$[\mathbf{R}\mu](s,\theta) = \int_{-\infty}^{\infty}\mu_\theta(s,\tau)d\tau. \tag{10}$$

Hereafter, we denote $\hat{s} = x\cos\theta + y\sin\theta$, $\hat{t} = y\sin\theta - x\cos\theta$ and $h(s,\theta) = [\mathbf{HR}\mu](s,\theta)$. With the above notations, the Novikov inversion formula is expressed as

$$f(x,y) = \frac{1}{4\pi}\int_0^{2\pi} e^{a_\theta(\hat{s},\hat{t})-0.5\mathbf{R}\mu(\hat{s},\theta)} \times\left\{\frac{\partial}{\partial s}\int_{-\infty}^{\infty}\frac{\cos\left(0.5\left[h(s,\theta)-h(l,\theta)\right]\right)}{\pi(s-l)} \times e^{0.5\mathbf{R}\mu(l,\theta)}\widetilde{p}(l,\theta)dl\right\}\Bigg|_{s=\hat{s}} d\theta. \tag{11}$$

Notice that formula (11) is slightly different from its original format in [2]. Formula (11) can be regarded as an operator, denoted by $\mathbf{N}_\mu\widetilde{p}$, from functions of $R^1\times S^1$ to functions of R^2. It was proved in [19] that the FBP-type algorithms in [9] and [10] can be derived as the special cases of (11).

The range condition for the aRT is to characterize the situation under which a data function $\widetilde{p}(s,\theta)$ indeed can be expressed as (3) for certain object function $f(x,y)$. More detailed description of the range condition can be found in [3], [20], and [21], and its application to the exponential Radon transform is reported in [22]–[24] and to the Radon transform is reported in [25]–[27]. In this paper, we adapt the general expression of the range condition from [3], which states that the attenuated Radon transform $p(s,\theta)$ must satisfy the following integral equation:

$$\int_0^{2\pi}\left[e^{0.5\mathbf{R}\mu(\hat{s},\theta)-a_\theta(\hat{s},\hat{t})}\int_{-\infty}^{\infty}\frac{\cos\left(0.5\left[h(\hat{s},\theta)-h(l,\theta)\right]\right)}{\pi(\hat{s}-l)} \times e^{0.5\mathbf{R}\mu(l,\theta)}p(l,\theta)dl\right]d\theta \equiv 0. \tag{12}$$

Due to the presence of noise, the measured projection data $\widetilde{p}(s,\theta)$ may not satisfy (12) in general, i.e., there might not exist any object function $f(x,y)$ such that $\widetilde{p}(s,\theta)$ is the aRT of $f(x,y)$. In the following, we apply the range condition to separate the noise $n(s,\theta)$ into two parts: one part satisfies the condition (12), and the other part does not.

Let $\Lambda = (-1,1)$, B be the unit disk of R^2, and $\boldsymbol{\chi}_\mathrm{B}$ be the characteristic function of B. From now on, we limit our discussion on the object function $f(x,y)$ with support in B for simplicity. For any function $g(s,\theta)$ of $\Lambda\times\mathrm{S}^1$, it can be decomposed into the following expression:

$$g(s,\theta) = [\mathbf{R}_\mu\boldsymbol{\chi}_\mathrm{B}\mathbf{N}_\mu g](s,\theta) + \{g(s,\theta) - [\mathbf{R}_\mu\boldsymbol{\chi}_\mathrm{B}\mathbf{N}_\mu g](s,\theta)\} \tag{13}$$

where the first term $[\mathbf{R}_\mu\boldsymbol{\chi}_\mathrm{B}\mathbf{N}_\mu]g$ must, from [2], [3], satisfy the range condition (12) since it is the aRT of $\boldsymbol{\chi}_\mathrm{B}\mathbf{N}_\mu g$. By the uniqueness of the aRT in [2], we have $[\boldsymbol{\chi}_\mathrm{B}\mathbf{N}_\mu]g = [\boldsymbol{\chi}_\mathrm{B}\mathbf{N}_\mu\mathbf{R}_\mu\boldsymbol{\chi}_\mathrm{B}\mathbf{N}_\mu]g$. This implies the following equality:

$$[\boldsymbol{\chi}_\mathrm{B}\mathbf{N}_\mu]\{g - [\mathbf{R}_\mu\boldsymbol{\chi}_\mathrm{B}\mathbf{N}_\mu]g\} \equiv 0. \tag{14}$$

Similarly, the noise $n(s,\theta)$ can also be decomposed into

$$n(s,\theta) = n_R(s,\theta) + n_N(s,\theta) \tag{15}$$

where

$$n_R(s,\theta) = [\mathbf{R}_\mu\boldsymbol{\chi}_\mathrm{B}\mathbf{N}_\mu n](s,\theta) \tag{16}$$

$$n_N(s,\theta) = n(s,\theta) - [\mathbf{R}_\mu\boldsymbol{\chi}_\mathrm{B}\mathbf{N}_\mu n](s,\theta). \tag{17}$$

The component $n_R(s,\theta)$ meets the condition (12) as the first term of (13) does. The component $n_N(s,\theta)$ belongs to the null space of the operator $\boldsymbol{\chi}_\mathrm{B}\mathbf{N}_\mu$ and does not meet condition (12). A more detailed description on the null space of the Radon transform operator was given in [20]. Hereafter, we call $n_R(s,\theta)$ the range-space noise and $n_N(s,\theta)$ the null-space noise. For the component $n_N(s,\theta)$, (14) becomes

$$[\boldsymbol{\chi}_\mathrm{B}\mathbf{N}_\mu n_N](x,y) \equiv 0. \tag{18}$$

Equation (18) implies that the null-space noise $n_N(s,\theta)$ has no contribution to the reconstructed image of the FBP-type algorithm (11). However, the null-space noise contributes to the ML-EM reconstructed image, although it could be reduced by the *a priori* penalty via the MAP criterion. In the following section, the null-space noise $n_N(s,\theta)$ is numerically found to be the major cause of the checkerboard artifacts in the ML-EM reconstruction. Removing the null-space noise could prevent the ML-EM reconstruction from divergence as the iteration goes up for noisy projection data. Here we want to specifically mention that an alternative decomposition of the null-space noise was investigated using the singular value decomposition (SVD) on the system matrix $\{c^{i,k}_{m,n}\}$ in [17].

V. Null-Space Noise Propagation

In this section, we perform numerical simulations to estimate the null-space noise and analyze its propagation to the recon-

structed image of the ML-EM algorithm. Assume that the emission distribution $f(x,y)$ and attenuation map $\mu(x,y)$ are defined inside the unit disk $x^2+y^2\le 1$. Functions $f(x,y)$ and $\mu(x,y)$ are evenly sampled in $[-1,1]\times[-1,1]$ on a grid of 128 $\times$ 128, and $[\mathbf{R}_\mu f](s,\theta)$ is evenly sampled in $[-1,1]\times[0,2\pi]$ on a grid of 128 $\times$ 128. All the emission phantom, attenuation map, and reconstructed images were linearly scaled to [0, 255] for display. The attenuated noise-free projections were calculated by line integrals given the emission phantom and attenuation map. In simulating the noisy projections, the Poisson number generator in [28] was used to generate the Poisson counts assuming the noise-free projections as their corresponding mean. In measuring the difference between images $I_1(m,n)$ and $I_2(m,n)$, the L^2 norm or mean-square error (MSE) was used, which has the following expression:

$$\mathrm{MSE}(I_1,I_2)=\sqrt{\sum\left(I_1(m,n)-I_2(m,n)\right)^2/(MN)} \quad (19)$$

where M and N are the image height and width, respectively. The L^2 norm of an image $I(m,n)$ is defined as

$$L^2(I)=\sqrt{\sum I^2(m,n)/(MN)}. \quad (20)$$

The signal-to-noise ratio (SNR) of an estimated image $I(m,n)$ against its mean image $S(m,n)$ is defined as

$$\mathrm{SNR}(I,S)=L^2(I)/\mathrm{MSE}(I,S). \quad (21)$$

A. Phantoms and Implementation of the ML-EM Algorithm

In all numerical simulations, $f(x,y)$ was chosen as the Shepp–Logan phantom, and $\mu(x,y)$ was similar to the phantom used in [19]. Their pictures are shown in Fig. 2. In order to identify any artifacts that the discontinuity of the emission object and the attenuation map might have, the attenuation map was designed to have different structures compared with the Shepp–Logan emission phantom so that the discontinuous edges in the Shepp–Logan phantom and the attenuation map are different. This is different from the phantoms used in [19].

Implementation of the ML-EM algorithm (7) can be carried out through two separate steps of reprojection and backprojection. In our numerical simulations, both the projector $\sum_{m,n} c_{m,n}^{i,k} f_{m,n}^{(j)}$ and the backprojector $\sum_{i,k} c_{m,n}^{i,k}\hat{p}_{i,k}$ were carried out in the detector coordinates $(s,t)_{\theta_k}$; here, $\hat{p}_{i,k}$ will be defined later. Let Δ and Ω denote the sampling interval for distance variables (x,y,s,t) and the angle variable θ, respectively. Assume that $(s_m,t_n)_{\theta_k}$ is evenly sampled for all variables. In the coordinate system $(s,t)_{\theta_k}$, the discrete projector becomes

$$\widetilde{p}_{i,k}^{(j)}=\sum_{m,n} c_{m,n}^{i,k} f_{m,n}^{(j)}=\Delta\sum_n f_{\theta_k}^{(j)}(s_i,t_n)e^{-a_{\theta_k}(s_i,t_n)} \quad (22)$$

where $a_{\theta_k}(s_i,t_n)=\Delta\sum_{j\ge n}\mu_{\theta_k}(s_i,t_j)$ and $f_{\theta_k}^{(j)}(s_i,t_n)$ was derived using the interpolation from $f_{m,n}^{(j)}$ as shown in Fig. 3. Recall that the coefficients $c_{m,n}^{i,k}$ in Section III were defined in

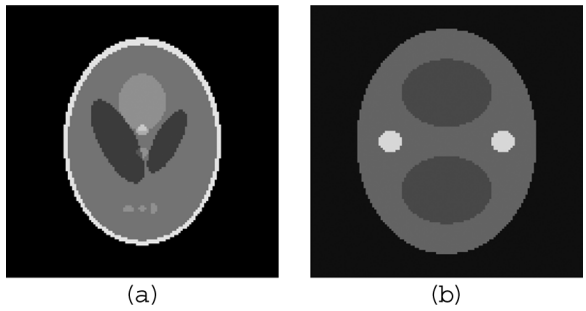

Fig. 2. (a) Shepp–Logan emission phantom and (b) attenuation map.

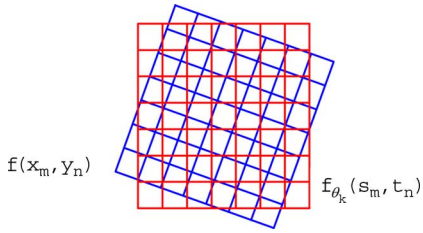

Fig. 3. Illustration of image rotation.

the coordinate (x,y). These coefficients vary depending on the selection of the initial coordinate system. Let ${}^{(\hat{k})}c_{m,n}^{i,k}$ be the contribution coefficients when $(s,t)_{\theta_{\hat{k}}}$ is the initial coordinate system. In the coordinate $(s,t)_{\theta_k}$, we observe that

$${}^{(k)}c_{m,n}^{i,k}=\Delta\delta_{i,m}e^{-a_{\theta_k}(s_m,t_n)} \quad (23)$$

here $\delta_{i,m}$ is the Kronecker's symbol. Let $f_{k;m,n}^{(j)}=f_{\theta_k}^{(j)}(s_m,t_n)$ be the estimate in the jth iteration. Notice that $f_{k;m,n}^{(j+1)}$ and $f_{m,n}^{(j+1)}$ can be derived from each other through rotation [29]–[31] and $\widetilde{p}_{i,k}^{(j)}$ can be calculated by (22). Define $\hat{p}_{i,k}=\widetilde{p}_{i,k}/\widetilde{p}_{i,k}^{(j)}$, we derive the expression of (7) in the coordinate $(s,t)_{\theta_k}$ as:

$$\sum_i c_{m,n}^{i,k}\hat{p}_{i,k}=\sum_i {}^{(k)}c_{m,n}^{i,k}\hat{p}_{i,k}=\Delta e^{-a_{\theta_k}(s_m,t_n)}\hat{p}_{m,k}. \quad (24)$$

Similarly we have $\sum_i c_{m,n}^{i,k}=\sum_i^{(k)} c_{m,n}^{i,k}=\Delta e^{-a_{\theta_k}(s_m,t_n)}$ under $(s,t)_{\theta_k}$. When restricted on the single direction $(\cos\theta_k,\sin\theta_k)$, (7) becomes

$$f_{k;m,n}^{(j+1)}=\frac{f_{k;m,n}^{(j)}}{\sum_i c_{m,n}^{i,k}}\sum_i c_{m,n}^{i,k}\frac{\widetilde{p}_{m,k}}{\sum_{m,n} c_{m,n}^{i,k}f_{k;m,n}^{(j)}}=f_{k;m,n}^{(j)}\hat{p}_{m,k}. \quad (25)$$

Actually, $\hat{p}_{i,k}$ in (25) generates a strip-like image in $(s,t)_{\theta_k}$. We averaged eight consecutive strip-like images $\hat{p}_{i,k}$ after rotation, and multiplied it to $f_{m,n}^{(j)}$ for $f_{m,n}^{(j+1)}$. Then we moved to the next eight consecutive directions until all the projections were visited. The whole procedure was repeated for the next EM iteration. Due to the use of rotation along each projection angle, the backprojector in (25) essentially does not need to involve the attenuation coefficients-related term $e^{-a_{\theta_k}(s_m,t_n)}$, which is slightly different from other implementations in the literature.

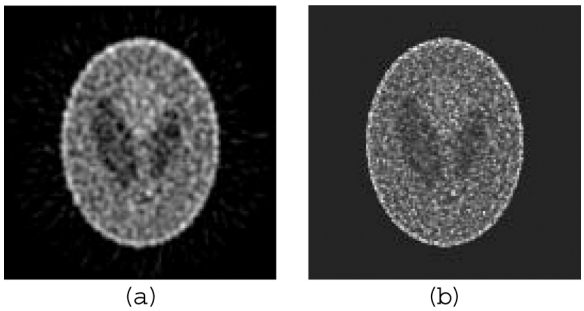

Fig. 4. The reconstructed images: (a) FBP and (b) OS-EM (4 iterations with OS size of 8).

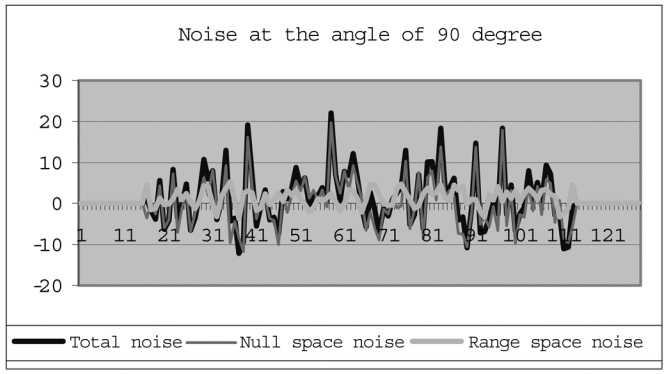

Fig. 5. Illustration of the total, null space and range space noises at the angle of 90°.

B. Estimate of the Null-Space Noise and Its Effect Upon the OS-EM Reconstruction

The Poisson counts for each detector bin were generated based on the corresponding mean projection, thus the total noise of all projections is known. Projections $p_{i,k}$ were sampled on a 128×128 grid in $[-1,1] \times [0,2\pi]$. Total counts were 650 K, and the SNR of the noisy projection data was 8.022, computed by (21). The numerical implementation of the Novikov's inversion formula (11) was used without any extra filtering [32]. For the noise-free data, the OS-EM and FBP-type methods virtually provide the same reconstruction in our simulations. For the noisy data, their reconstructions look quite different as shown in Fig. 4. The OS-EM algorithm was run up to ten iterations from a uniform initial and the result from the fourth iteration seems to give the highest SNR among the ten iterated results although the image from the third iteration looks smoother than the one from the fourth iteration. The results were smoother before and diverged after four iterations, concurring with the previous studies, e.g., [4]. The SNRs of the reconstructed images by the FBP-type and OS-EM algorithms were 3.60 and 2.59, respectively. Both the SNRs and Fig. 4 reveal that the OS-EM algorithm generates noisier results than the FBP-type algorithm. Certainly, the noise came from both components $n_R(s,\theta)$ and $n_N(s,\theta)$. In this paper, we intend to study their different propagation effects in their reconstructed images. The extra noise in the OS-EM reconstruction was assumed due to the null-space noise, as discussed at the end of Section IV. This assumption was further validated by the study below.

Next, we estimate the null-space noise $n_N(s_i,\theta_k)$ from the known total noise $n(s_i,\theta_k)$ in discrete space. Theoretically, this could be done by solving equation system (12), but it may not be practical numerically. Using $p = [\mathbf{R}_\mu \boldsymbol{X}_{\mathrm{B}} \mathbf{N}_\mu]p$ and (4), (15) and (16), we have the following equality:

$$n_N(s,\theta) = \widetilde{p}(s,\theta) - [\mathbf{R}_\mu \boldsymbol{X}_{\mathrm{B}} \mathbf{N}_\mu \widetilde{p}(s,\theta)]\,(s,\theta). \tag{26}$$

Equation (26) implies that the null-space noise can be estimated and removed through reprojecting the reconstructed image by (3) and (11). The estimate of $n_N(s_i,\theta_k)$ takes the following steps: i) reconstructing the noisy data $\widetilde{p}_{i,k}$ by (11) to obtain the image $f_0(x_m,y_n) = \boldsymbol{X}_{\mathrm{B}} \mathbf{N}_\mu \widetilde{p}(s,\theta)$; ii) reprojecting $f_0(x_m,y_n)$ by (3) to derive $\widetilde{p}_R(s_i,\theta_k) = \mathbf{R}_\mu f_0(x_m,y_n)$; and iii) computing the null-space noise $n_N(s_i,\theta_k) = \widetilde{p}_{i,k} - \widetilde{p}_R(s_i,\theta_k)$. Let $f_1(x_m,y_n)$ be the reconstructed image from the same noisy projection $\widetilde{p}_{i,k}$ by the OS-EM algorithm [7]. It is noted that $f_0(x_m,y_n)$ is the image of Fig. 4(a) and $f_1(x_m,y_n)$ is the image of Fig. 4(b). For rotation angle $\theta_k = 90°$, the estimated $\widetilde{p}_R(s_i,\theta_k)$ and $n_N(s_i,\theta_k)$ using the procedure above are displayed in Fig. 5. The original noisy projection $\widetilde{p}_{i,k}$ is also displayed in Fig. 5 for comparison. Note that the estimated $\widetilde{p}_R(s_i,\theta_k)$ and $n_N(s_i,\theta_k)$ may contain numerical errors. In the subsequent analysis, we assume that the numerical errors can be ignored compared with the actual null-space noise.

Recall that the SNR of $\widetilde{p}_{i,k}$ against the mean projection $p_{i,k}$ is 8.022. When the regenerated projection $\widetilde{p}_R(s_i,\theta_k)$ was assumed as the mean projection, the estimated SNR of $\widetilde{p}_{i,k}$ against $\widetilde{p}_R(s_i,\theta_k)$ is 8.021, which is very close to the actual SNR of 8.022. This observation may suggest that $\widetilde{p}_R(s_i,\theta_k)$ may be a good approximation of the unknown mean projection $p_{i,k}$. Actually, the relation $\mathrm{MSE}(n,n_R)/L^2(n) = 1.02$ supports this suggestion. Moreover, $\mathrm{MSE}(n,n_N)/L^2(n) = 0.38$ implies that the null-space noise $n_N(s,\theta)$ is the major component in the total noise $n(s_i,\theta_k)$. From these calculations and Fig. 5, the null-space noise is clearly seen as the dominant component. Similar numerical simulation results were observed in other noise levels and different emission phantoms and attenuation maps.

By (26), the reprojected data $\widetilde{p}_R(s_i,\theta_k) = \widetilde{p}_{i,k} - n_N(s_i,\theta_k)$ does not contain the null-space component, and its SNR against the original projection $\widetilde{p}_{i,k}$ becomes 21.01. This means that (26) can be used to filter the null-space noise and the removal of the null-space noise could significantly improve the SNR of the data. Now we may treat the less noisy projection $\widetilde{p}_R(s_i,\theta_k)$ as the data consistent to the image to be sought. Reconstructing the image can be performed by either analytical or iterative algorithms.

Equation (14) implies that the analytical FBP-type reconstructed image from $\widetilde{p}_{i,k}$ and $\widetilde{p}_R(s_i,\theta_k)$ should be the same after ignoring numerical errors. In other words, removing the null-space noise does not improve the FBP-type reconstruction at all, which can be seen from Fig. 6(a). The SNRs of the FBP-type reconstructed images from $\widetilde{p}_R(s_i,\theta_k)$ was slightly increased to 3.71.

To the authors' knowledge, it is unclear whether an association, similar to (14) for the analytical FBP-type algorithm, exists between the range condition of the aRT and the iterative ML-EM algorithm. This is investigated numerically in this study. We reconstructed $\widetilde{p}_R(s_i,\theta_k)$ using the OS-EM algorithm

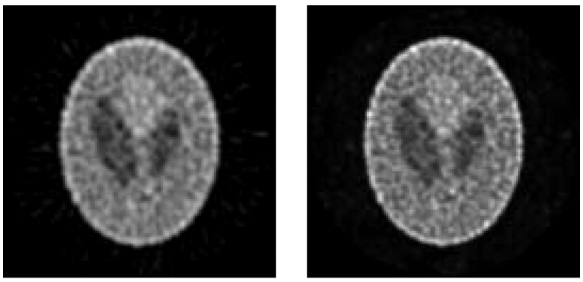

Fig. 6. Reconstructed images after removing the null-space noise: (a) FBP-type and (b) OS-EM (four iterations with OS size of 8) algorithms.

and found that removing the null-space noise from the original noisy projection does improve the OS-EM reconstruction noticeably as shown in the Fig. 6(b). We ran the OS-EM algorithm up to 20 iterations from a uniform initial and the results after four iterations were very stable, virtually without any change. In other words, removing the null-space noise stabilizes the OS-EM iterative reconstruction. The SNR of the OS-EM reconstructed image from $\widetilde{p}_R(s_i, \theta_k)$ was 4.04, which is a noticeable improvement compared with 2.59 of the OS-EM reconstruction from the original noisy projection data $\widetilde{p}_{i,k}$. The severe checkerboard artifacts in Fig. 4(b) are reduced noticeably, as seen in Fig. 6(b). This would suggest that the null-space noise may be the major cause of the severe checkerboard artifacts in the OS-EM or ML-EM algorithm.

VI. Discussion and Conclusion

This study investigated the checkerboard artifacts of the ML-EM reconstruction algorithm by the use of the range condition of the attenuated Radon transform. The Novikov's inversion formula was used to separate the null-space noise component from the original projection noise. The null-space noise was observed to dominate the total data noise. It was further shown that the null-space noise does not contribute to the noise propagation in the FBP-type reconstruction, but plays a significant role in the noise propagation in the ML-EM iterative reconstruction. The null-space noise was observed as the major cause of the severe checkerboard artifacts. Removing the null-space noise stabilized the OS-EM iteration.

Characterizing and filtering the range-space noise would be a major task for FBP-type analytical reconstruction and remains an interesting research topic. Estimating and removing the null-space noise could significantly improve the ML-EM reconstruction without *a priori* penalty. Use of the reprojection of the FBP-type result to estimate the null-space noise could be one choice, but is not very practical. The SVD method may be an alternative to estimate the null-space noise by using the system matrix coefficients $c^{i,k}_{m,n}$ as shown in [17]. This is worth for further investigation since the SVD method may help deal with other image degradation factors such as collimator response and scattering.

It was proved in [26] that forcing the projection data to be consistent with the Radon transform, by $\min \|p_N(s,\theta)\|_{L^2}$ such that $p(s,\theta) = \widetilde{p}(s,\theta) + p_N(s,\theta)$ satisfies (12), does not help much for noise reduction in the FBP-type inversion methods. This study confirms that removing the null-space noise by the range condition does not help the noise reduction when using the inverse aRT because the null-space noise annihilates during the reconstruction. Within the analytical reconstruction, it seems that the only way to reduce the reconstruction noise is to reduce the range-space noise.

Most, if not all, of the previous noise reduction approaches in the literature deal with the data noise as a whole for both analytical inversion and iterative update reconstructions. This study explored an alternative strategy to separate the noise into two components and consider their noise effects separately. Efficient means for estimating the null-space noise remains a research topic, although this study and others [17] have made progress. This is because removing the null-space noise would stabilize the OS-EM iteration so that compensation for the attenuation, scatter, collimator response and other degradation factors can be achieved under an effective control of the Poisson noise.

References

[1] G. T. Gullberg, "The Attenuated radon transform: Theory and application in medicine and biology," Ph.D. dissertation, Donner Laboratory, Univ. of California, Berkeley, CA, 1979.
[2] R. G. Novikov, "An inversion formula for the attenuated X-ray transformation," *Ark. Math.*, vol. 40, pp. 145–167, 2002, Preprint, May 2000.
[3] R. G. Novikov, "On the range characterization for the two-dimensional attenuated X-ray transformation," *Inverse Problems*, vol. 18, pp. 677–700, 2002.
[4] D. Snyder, M. Miller, L. Thomas, and D. Politte, "Noise and edge artifacts in ML reconstruction for emission tomography," *IEEE Trans. Med. Imag.*, vol. 6, no. 3, pp. 228–238, Sep. 1987.
[5] A. Dempster, N. Laird, and D. Rubin, "Maximum likelihood from incomplete data via the EM algorithm," *J. R. Stat. Soc. Series B*, vol. 39B, pp. 1–38, 1977.
[6] L. A. Shepp and Y. Vardi, "Maximum likelihood reconstruction for emission tomography," *IEEE Trans. Med. Imag.*, vol. 1, no. 2, pp. 113–122, Oct. 1982.
[7] H. M. Hudson and R. S. Larkin, "Accelerated image reconstruction using ordered subsets of projection data," *IEEE Trans. Med. Imag.*, vol. 13, no. 4, pp. 601–609, Dec. 1994.
[8] A. Papoulis, *Probability, Random Variables, and Stochastic Processes*, 2nd ed. New York: McGraw-Hill, 1984.
[9] L. A. Shepp and B. Logan, "The Fourier reconstruction of a head section," *IEEE Trans. Nucl. Sci.*, vol. 21, pp. 21–43, Jun. 1974.
[10] O. Tretiak and C. E. Metz, "The exponential Radon transform," *SIAM J. Appl. Math.*, vol. 39, pp. 341–354, 1980.
[11] R. Gordon, R. Bender, and G. T. Herman, "Algebraic reconstruction techniques (ART) for three dimensional electron microscopy and X-ray photography," *J. Theory Biol.*, vol. 29, pp. 471–481, 1970.
[12] H. Hart and Z. Liang, "Bayesian image processing in two dimensions," *IEEE Trans. Med. Imag.*, vol. 6, no. 3, pp. 201–208, Sep. 1987.
[13] H. H. Barrett, D. W. Wilson, and B. M. W. Tsui, "Noise properties of the EM algorithm: I. Theory," *Phys. Med. Biol.*, vol. 39, pp. 833–846, 1994.
[14] D. W. Wilson, B. M. W. Tsui, and H. H. Barrett, "Noise properties of the EM algorithm: II. Monte Carlo simulations," *Phys. Med. Biol.*, vol. 39, pp. 847–871, 1994.
[15] J. A. Fessler, "Mean and variance of implicitly defined biased estimators (such as penalized maximum likelihood): Applications to tomography," *IEEE Trans. Imag. Process.*, vol. 5, no. 3, pp. 493–506, Mar. 1996.
[16] W. Wang and G. Gindi, "Noise analysis of MAP-EM algorithms for emission tomography," *Phys. Med. Biol.*, vol. 42, pp. 2215–2232, 1997.
[17] D. W. Wilson and H. H. Barrett, "Decomposition of images and objects into measurement and null components," *Opt. Exp.*, vol. 2, pp. 254–260, 1998.
[18] J. Qi and R. M. Leahy, "Resolution and noise properties of MAP reconstruction for fully 3D PET," *IEEE Trans. Med. Imag.*, vol. 19, no. 5, pp. 493–506, May 2000.
[19] L. A. Kunyansky, "A new SPECT reconstruction algorithm based on the Novikov explicit inversion formula," *Inverse Problems*, vol. 17, pp. 293–306, 2001.

[20] A. K. Lious, "Orthogonal function series expansions and the null space of the Radon transform," *SIAM J. Math. Anal.*, vol. 15, pp. 621–633, 1984.

[21] F. Natterer, *The Mathematics of Computerized Tomography*. New York: Wiley-Teubner, 1986.

[22] V. Aguilar, L. Ehrenpreis, and P. Kuchment, "Range conditions for the exponential Radon transform," *J. d'Analyse Mathematique*, vol. 68, pp. 1–13, 1996.

[23] V. Aguilar and P. Kuchment, "Range conditions for the multidimensional exponential X-ray transform," *Inverse Problems*, vol. 11, pp. 977–982, 1995.

[24] O. Öktem, "Extension of separately analytic functions and applications to range characterization of the exponential Radon transform," *Ann. Polon. Math.*, vol. 70, pp. 195–213, 1998.

[25] I. Ponomarev, "Correction of emission tomography data: Effects of detector displacement and non-constant sensitivity," *Inverse Problems*, vol. 10, pp. 1–8, 1995.

[26] F. Natterer, "Range condition in tomography," Technical Note, 1999 [Online]. Available: http://wwwmath1.uni-muenster.de/num/Preprints/2004/natterer_2

[27] M. A. Anastasio, X. Pan, and E. Clarkson, "Comments on the filtered backprojection algorithms, range conditions, and the pseudoinverse solution," *IEEE Trans. Med. Imag.*, vol. 20, no. 6, pp. 539–542, Jun. 2001.

[28] W. H. Press, S. A. Teukolsy, W. T. Vetterling, and B. P. Flannery, *Numerical Recipes in C*. Cambridge, U.K.: Cambridge Univ. Press, 1992.

[29] J. Ye, Z. Liang, and D. P. Harrington, "Quantitative reconstruction for myocardial perfusion SPECT: An efficient approach by depth-dependent de-convolution and matrix rotation," *Phys. Med. Biol.*, vol. 39, pp. 1263–1279, 1994.

[30] E. Dibella, A. Barclay, R. Eisner, and R. Schaefer, "A comparison of rotation-based methods for iterative reconstruction algorithms," *IEEE Trans. Nucl. Sci.*, vol. 43, no. 6, pp. 3370–3376, Dec. 1996.

[31] J. W. Wallis and T. R. Miller, "An optimal rotator for iterative reconstruction," *IEEE Trans. Med. Imag.*, vol. 16, no. 1, pp. 118–123, Feb. 1997.

[32] J. You, T. Li, and Z. Liang, "A classical FBP implementation of Novikov's inversion formula for quantitative SPECT imaging," IRIS Lab, SUNY, Stony Brook, NY, Mar. 2004, Tech. Rep.